

# A Robust Eye-Corner Detection Method for *Real-World* Data

Gil Santos and Hugo Proença

**Abstract**—Corner detection has been motivating several research works and is particularly important in different computer vision tasks, acting as basis for further image understanding stages. Particularly, the detection of eye-corners in facial images is relevant for domains such as biometric systems and assisted-driving systems. Having empirically evaluated the state-of-the-art of eye-corner detection proposals, we observed that they only achieve satisfactory results when dealing with good quality data. Hence, in this paper we describe an eye-corner detection method with particular focus on robustness, i.e., the suitability to deal with degraded data, toward the applicability in *real-world* conditions. Our experiments show that the proposed method outperforms others either in noise-free and degraded data (blurred, rotated and with significant variations in scale), which is regarded as the main achievement.

## I. INTRODUCTION

A corner is defined by the intersection of at least two edges. For decades, it was believed that most primitives of the human visual system were based in the detection of such type of interest points, which have a well-defined position. Corner detection is known to have particular relevance in computer vision, as it is often used as starting point to other image understanding processes. Hence, different corner detection strategies were previously reported in image segmentation, tracking, recognition and motion detection systems.

In this paper we are particularly interested in the detection of both the temporal and nasal eye-corners of facial images. Eye-corners constitute relevant keypoints and the ability to accurately pinpoint them is of great value in domains such as biometrics and driving assistance systems. In the case of biometrics, an emerging type of recognition is called *periocular* and refers to the human recognition by making use of data located in the vicinity of the eyes. The periocular region is particularly useful when the quality of data diffcults other recognition strategies: for un-cooperative subjects, using visible light imagery and acquiring data from moving subjects at-a-distance (e.g., [12], [10], [9], [15]).

Above all keypoints able to be extracted from the periocular region, we highlight eye-corners – the interceptions between the upper and lower eyelids – as their position is invariant to expression, levels of eye closure, gazed look, eyelash and makeover. Having analyzed the state-of-the-art about eye-corner detection, we concluded that published methods lack of robustness and were devised to operate

in good quality data. Moreover, we empirically observed that these approaches tend to significantly deteriorate their performance in *real-world* data, which heterogeneity is significantly higher. Hence, this work proposes an eye-corner detection method suitable for harsher environments, such as uneven lighting conditions, rotated or blurred data, with notorious differences in scale and levels of eye closure. Our method uses as input a periocular image, segments the iris and the sclera and defines a region-of-interest from where candidate points are extracted. Then, multiple features are linearly combined in an objective function which optimization determines the pair of points deemed to constitute the nasal and temporal eye-corners.

### A. Related Work

Several approaches for the detection of eye corners can be found in the literature: Harris and Stephens [6] proposed a corner detection method of general purposes, which is often used in the specific case of eye-corners with satisfactory results in good quality data. Zheng *et al.* [17] estimated an initial region-of-interest from integral projections and located eye-corners according to a bank of Gabor-based filters, convolved at five different scales and orientations, which averaged outputs yielded the final detection kernel. A deepen description of this strategy can be found in [18]. Khosravi and Safabakhsh [7] localized eye-corners in gray data, starting from the deemed center of the iris and selecting two points on its scleric boundary at symmetric angles. Next, they found points on eyelids, according to local differences in brightness, and used four masks to define motion direction. Xu *et al.* [16] used the approach of Harris to select candidate points, and then parsed them combining semantic features using logistic regression. However, this method relies on image edges, hard to obtain in unconstrained acquisition environments. Haiying and Gouping [5] propose the weighting of Harris' response function with the variance projection function, achieving a more robust system for frontal images with no significant lighting variations nor rotation. The variance projection function itself was proposed for similar purposes by Feng and Yuen [4]. More recently, Erdogmus and Dugelay [3] proposed a method that achieves good results on frontal images, but also heavily relies on edge detection, and eye-corners result from the interception of polynomial functions fitted to these edges.

The remaining of this paper is organized as follows: in Section II we describe our method with detail; Section III

presents our experiments and discusses the obtained results, with emphasis to the robustness factor. Finally, Section IV states the conclusions.

## II. PROPOSED METHOD

### A. Iris Segmentation and Definition of the Region-Of-Interest

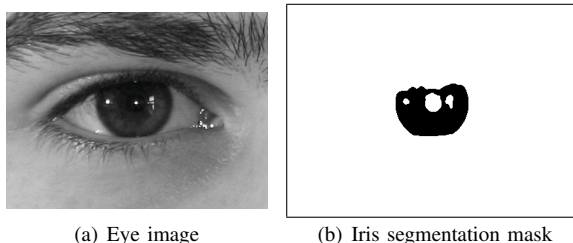


Fig. 1. Data used as input by our method.

As illustrated in figure 1, our method receives as input a periocular image and the first step is to obtain the corresponding noise-free iris binary segmentation mask. This mask discriminates between the noise-free regions of the iris and all the remaining data and was obtained as described by Tan *et al.* [14], which is known to operate in *real-world* data. Also, this iris segmentation algorithm was selected because it outperformed in the NICE.I contest <sup>1</sup>. The segmented iris data is represented by black regions of figure 1(b) and contain holes that correspond to the pupil and to occluded iris regions. These holes were removed by zeroing out all the regions unreachable when filling out the background from the edges of the image, as described in [13].

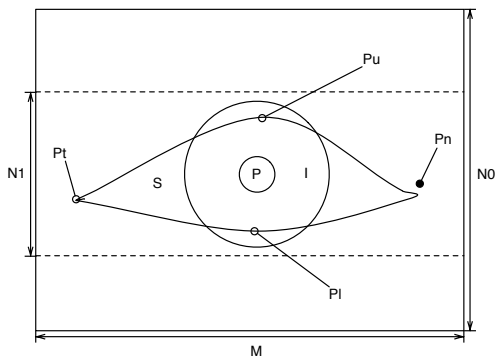


Fig. 2. Illustration of the regions of the eye evolved in our work.  $P$ ,  $I$  and  $S$  correspond to the pupil, iris and sclera.  $P_n$  and  $P_t$  are the nasal and temporal eye-corners.  $P_u$  and  $P_l$  are both extremes of the region segmented as iris, which were used by the proposed method.

Next, we aimed at defining a region-of-interest (ROI), from where subsequent processing should be done. This region is illustrated in figure 2 and was obtained by cropping the input image and the segmentation mask, avoiding unneeded regions, such as the eyebrow and skin underneath the eye. Having an input image of dimensions  $M \times N_0$ , this yields regions of  $M \times N_1$  dimensions, according to horizontal

<sup>1</sup>NICE.I: Noisy Iris Challenge Evaluation - Part I <http://nice1.di.ubi.pt>

projection techniques and assuring that the ROI comprises the extreme coordinates of pixels belonging to the iris ( $P_s$  and  $P_i$  of Figure 2):

$$\begin{aligned} y_u &= \max(y_p) \\ y_l &= \min(y_p) \end{aligned} \quad (1)$$

where  $y$  are the row coordinates of all the pixels that belong to the iris, obtaining ROIs similar to the illustrated in Figure 3. To account for rotated data, the input images and the corresponding iris segmentation masks were previously rotated, so that the major axis of the iris regions became horizontal, as it is known that lateral regions of the iris are less susceptible to occlusions and that most of the times that major axis will correspond to the direction of eye-corners.

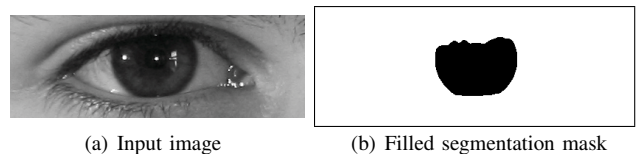


Fig. 3. Initial ROI and corresponding filled iris segmentation mask.

### B. Sclera Segmentation

The localization of regions that correspond to the sclera inside the ROI is a key issue of our method, as both eye corners should be adjacent to the sclera. Also, it is known that pixels belonging to the human sclera have particularly low levels of saturation, which is illustrated by figure 4. This left image gives the saturation channel of the HSV colorspace (Figure 4(a)), and the right one shows the result of the convolution with an unidimensional horizontal median filter [8] for eyelash attenuation, followed by data quantization and histogram equalization (Figure 4(b)). From this example, it is notorious that sclera were turned more homogenous and with evidently lower intensities, enabling its classification by empirically adjusted thresholds.

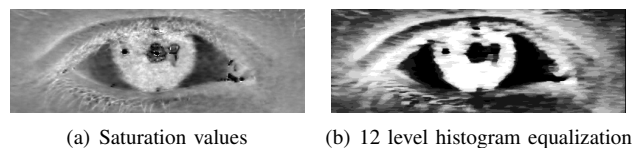


Fig. 4. Sclera enhancement.

### C. Eye Contour Approximation

Having segmented the iris and sclera, the next stage comprises the approximation of the eyelids contour. This was performed in two steps: 1) morphological dilation of the iris segmentation mask with an horizontal structuring element, which will horizontally *expand* the iris regions and 2) point-by-point multiplication between the dilated and the enhanced data illustrated in figure 4(b), as described by Caselles [2], obtaining images similar to the illustrated in figure 5(b), and which boundary constitutes a good approximation to the eyelids contour.



Fig. 5. The deemed eyelid contour corresponds to the boundary of the region signaled by black pixels.

#### D. Generation of Eye-Corner Candidates

This stage comprises the generation of a set of candidate points for the position of eye-corners, which was performed by using the approach of Harris and Stephens [6]. However, having observed a high probability of producing too many false positives, this detector was exclusively applied inside the nasal ( $R_n$ ) and temporal ( $R_t$ ) regions, cropped from the extremes of the major axis of the sclera mask, as illustrated in figure 6).



Fig. 6. Approximation of the eyelid contour (white snake) and regions from where corner candidates are extracted (represented by white rectangles).

#### E. Feature Set

This stage aims at finding appropriate features to discriminate between the set of corner candidates. Also, it constituted our concern that such feature set would be robust to differences in translation, rotation, scale, affine-transform and blurred data. In all subsequent descriptions, we consider  $\{c_i\}_{i=1}^n$ ,  $c_i = (x_i, y_i)$ , the set of eye-corners candidates.

a) *Harris Pixel Weight*  $H(P_c)$ : Considering that all candidates were generated according to the Harris and Stephens method, it is straightforward to include the corresponding score in the proposed feature set. This score is given by:

$$H = |M| - k \operatorname{tr}(M)^2 \quad (2)$$

where  $|\cdot|$  denotes matrix determinant,  $\operatorname{tr}(\cdot)$  is the trace of a matrix and  $M$  is the Hessian matrix obtained from a blurred version of the original data:

$$M(x, y) = \begin{bmatrix} G_u^2(x, y) & G_{uv}(x, y) \\ G_{uv}(x, y) & G_v^2(x, y) \end{bmatrix}$$

being  $G(x, y) = I(x, y) \otimes h(x, y)$ , with  $h(x, y) = \frac{1}{2\pi} \exp\left(-\frac{x^2+y^2}{2}\right)$  and  $\otimes$  denotes convolution.

b) *Internal Angles*: Let  $B = \{b_i\}_{i=1}^k$ ,  $b_i = (x_i, y_i)$  be the set of pixels belonging to the eyelid boundary, obtained as described in section II-C. An ellipse fitted to  $B$  points is parameterized in the following way:

$$E = (x_e, y_e) + Q(\gamma) \cdot \begin{bmatrix} A \cdot \cos(\sigma) \\ B \cdot \sin(\sigma) \end{bmatrix} \quad (3)$$

where  $(x_e, y_e)$  is the ellipse central point,  $Q(\gamma)$  a rotation matrix and  $A$  and  $B$  are the lengths for the major and minor axis respectively. Two sets of pixels located along the opposite directions of the ellipse's minor axis are given by:

$$b_l = \left(x_e - \cos\left(\gamma - \frac{\pi}{2}\right) \cdot B, y_e - \sin\left(\gamma - \frac{\pi}{2}\right) \cdot B\right) \quad (4a)$$

$$b_u = \left(x_e + \cos\left(\gamma - \frac{\pi}{2}\right) \cdot B, y_e + \sin\left(\gamma - \frac{\pi}{2}\right) \cdot B\right) \quad (4b)$$

For every candidate point  $c_i$ , two vectors  $\vec{u} = c_i - b_u$  and  $\vec{v} = c_i - b_l$  were obtained (Fig. 7), and their internal angle  $\theta(c_i, E)$  given by:

$$\theta_1(c_i, E) = \arccos\left(\frac{\langle u, v \rangle}{\|u\| \cdot \|v\|}\right) \quad (5)$$

where  $\langle u, v \rangle$  is the dot product between  $u$  and  $v$ , and  $\|\cdot\|$  denotes the norm of a vector.

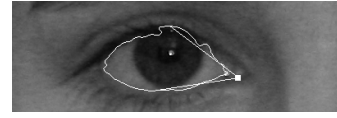


Fig. 7. Approximation of the eye contour (white snake). Example of a candidate point and of the vectors from where the internal angle  $\theta_1(c_i, E)$  is obtained.

Let  $m_1$  be the slope of the ellipse major axis, and  $m_2$  the slope of the line connecting  $(x_e, y_e)$  and the candidate point  $c_i$ :

$$m_2 = \frac{y_e - y_i}{x_e - x_i} \quad (6)$$

Their internal angle measures the agreement between the directions of the ellipse major axis and the straight line that passes in the candidate point and ellipse center:

$$\alpha_2(c_i, E) = \arctan\left(\frac{m_2 - m_1}{1 + m_1 \cdot m_2}\right) \quad (7)$$

Finally, considering that we are interested in pairs of eye corners, we found useful to obtain a feature that relates any two candidates as a pair, instead of scoring them independently. Let  $c_{i1}$  and  $c_{i2}$  be two corner candidates, one from the temporal and other from the nasal region and  $l_{12}$  the line that passes through both points. If the plausibility of both candidates is high, the direction of  $l_{12}$  should be similar to that of the major axis of the previously defined ellipse  $E$ . Thus, according to (7), we obtained the internal angle between these vectors ( $\alpha_3(c_{i1}, c_{i2}, E)$ ).

c) *Positions in ROIs*: A complementary type of features measures the relative position of each candidate in the ROIs, i.e., the proportion of pixels inside the ROI that are above each candidate. This feature is given by:

$$p(c_i, R) = \frac{\sum_{i=x_i}^{N_1} \sum_{j=1}^M \mathbb{I}_{\{(i,j) \in R\}}}{\sum_{i=1}^{N_1} \sum_{j=1}^M \mathbb{I}_{\{(i,j) \in R\}}} \quad (8)$$

where  $\mathbb{I}_{\{\cdot\}}$  is an indicator function.

d) *Relative Distances*: This type of feature considers the distance between each candidate point  $c_i$  and the ellipse center:

$$d_1(c_i, E) = \frac{\sqrt{(x_i - x_e)^2 + (y_i - y_e)^2}}{A} \quad (9)$$

where  $(x_e, y_e)$  denotes the coordinates of the center of the ellipse and  $A$  the length of the ellipse major axis, to compensate for the imbalance in acquisition distance and eye size

Let  $\vec{v}_a$  be a vector with the same direction of the major axis of the ellipse and  $p_1 = (x_1, y_1)$  and  $p_2 = (x_2, y_2)$  be the antipodal points of the ellipse. Let  $p_{tan} = (x_{tan}, y_{tan})$  be a point tangent to the ellipse that belongs to a line that passes through  $c_i$ :

$$\begin{aligned} x_{tan} &= x_1 + u(x_2 - x_1) \\ y_{tan} &= y_1 + u(y_2 - y_1) \end{aligned} \quad (10)$$

being  $u$  given by:

$$u = \frac{(x_c - x_1)(x_2 - x_1) + (y_c - y_1)(y_2 - y_1)}{\|p_2 - p_1\|^2}$$

The Euclidean distance between  $p_{tan}$  and each candidate  $c_i$  ( $d_2(c_i, p_{tan})$ ) was also added to the feature set.

e) *Interception of Interpolating Polynomials*: The nasal and temporal eye corners can be regarded as the interceptions between the upper and lower eyelids. Due to this, we parameterized two lines, each one corresponding to one eyelid. The interceptions  $t$  of both polynomials are illustrated by figure 8 and give a rough estimate of the nasal and temporal eye corners. According to our observations about the typical shape of eyelids, we decided to use second and third degree polynomials to fit the contours from the lower and upper eyelid. Thus, the Euclidean distance between each candidate and the interception point of the corresponding ROI ( $d_3(c_i, t)$ ) also acts as a measure of goodness for each candidate.

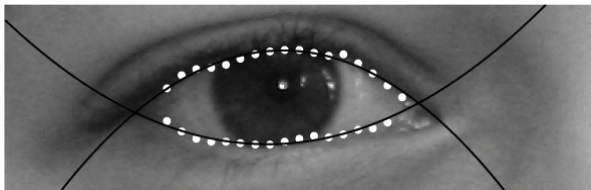


Fig. 8. Interpolating polynomials of order two (lower eyelid) and three (upper eyelid). The interception points of both polynomials constitute a good approximation to the eye corners.

#### F. Objective Function

According to the description given in section II-E, the proposed feature set is composed by seven features  $F = \{h(c_i), \theta_1(c_i, E), \theta_2(c_i, E), p(c_i, R), d_1(c_i, E), d_2(c_i, E), d_3(c_i, p_{tan}), d_3(c_i, t)\}$ , which should be fused to produce the final score. Having two sets of corner candidates (nasal

and temporal), the final score for every pair of nasal  $c_n$  and temporal  $c_t$  candidates is given by the weighted sum of these features:

$$\Gamma(c_t, c_n) = \sum_{i=1}^7 \beta_i f_i + \sum_{j=8}^{14} \beta_j f_{j-7} \quad (11)$$

where  $\{\beta_1, \dots, \beta_{14}\}$  are regularization terms adjusted to maximize performance in a training set. This optimization procedure was handled by linear regression and these terms were adjusted so to minimize the mean squared error between the predicted values and the ground-truth data, using Akaike criterion [1]:

$$J(c_t, c_n) = (\Gamma(c_t, c_n) - g(c_t, c_n))^2 \quad (12)$$

where  $g(c_t, c_n)$  is the sum of the Euclidean distances between the coordinates of the candidates and the ground-truth data.

### III. EXPERIMENTS

#### A. Datasets

The performance of the proposed method was assessed on right-eye images of the UBIRIS.v2 database [11]. Images have dimensions  $400 \times 300$ , were acquired from moving subjects, in visible wavelengths, at different distances and varying lighting conditions. Also, their quality is degraded by different factors, such as blur, motion, rotation and gaze. In order to check the degradation in performance with respect to each factor, five dataset configurations were used and are illustrated in Figure 9:

- *Frontal* – contains 300 images with the subjects gaze aligned to the camera;
- *Deviated Gaze* – 200 images where the subjects' head was deviated;
- *Blur* – images with an artificially made 50 pixel length motion blur, in  $\pi/4$  direction;
- *Clockwise rotation (CR)* – images artificially rotated by  $\pi/8$  clockwise;
- *Counter-clockwise rotation (CCR)* – same as the previous, with counter-clockwise rotation.

For the *Blur*, *CR* and *CCR* experiments, selected images of the UBIRIS.v2 were not enough and variations were artificially made by image processing software, starting from the *frontal* subset. For all images, the ground-truth data was manually made by different experts, in order to reduce subjectivity.

#### B. Results

According to the analysis to the previously published research works, the type of data they aim to deal with and the results given by authors, we decided to compare the performance of our method to the Haiying and Guoping [5] and Erdogmus and Dugelay [3] strategies. Also, as we found that one of the proposed features (Interception of polynomials) constitutes a strong estimator even when used alone, we decided to include it in our comparisons (Polyfit

I.). All the error values given in this section correspond to the Euclidean distance between the estimated location for the eye-corners and the *true* location, obtained by manual annotation of all the images in our datasets.

Figure 10 gives the results obtained for frontal images, which is clearly the data subset that appearance that most closely resemble the type of data the other methods aim to deal with. Fig. 10(a) gives the global detection rates and Figures 10(b) and 10(c) specifies the results obtained for the temporal and nasal eye-corners. The horizontal axes denote the error values and the vertical axes give the proportion of images with at most the corresponding error. From its analysis, it is evident that the proposed approach clearly outperformed in frontal images. If the analysis is performed separately for nasal and temporal corners, we observed that for the temporal region the polynomial interpolation was better than the Erdogmus and Dugelay method, and in most cases comparable to the proposed method. Regarding the nasal corners, we observed that all methods behave similarly for small error values, whereas our proposal is notoriously better for moderate and large error values (larger than 25 pixels).

For comprehensibility purposes, Figure 11 compares the boxplots of the error values observed for the proposed method and others used as comparison term, in the temporal (black bars) and nasal (gray bars) corners. We show the median of the observed performance range (horizontal solid lines) and the first and third quartile values of the observations (top and bottom of the box marks). The upper and lower whiskers are denoted by the horizontal lines outside each box, and the outliers are denoted by dot points. This plots highlights that methods are generally more efficient in detecting the nasal eye-corner, with exception to the Erdogmus and Dugelay strategy. Again, the better performance of our proposal, when compared to others, is evident.

Another interesting analysis comprises the levels of correlation between the outputs given by the compared strategies. Here, we assumed that correlation will at most be linear,

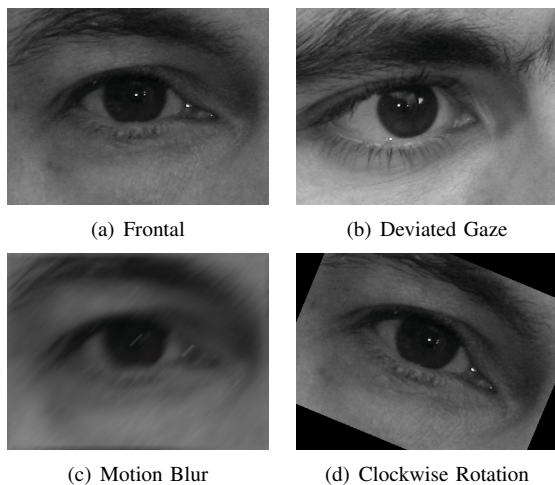


Fig. 9. Sample images from the different datasets.

TABLE I  
PEARSON'S CORRELATION COEFFICIENTS BETWEEN THE COMPARED METHODS.

	<i>Proposed</i>	<i>Polyfit I.</i>	<i>Haiying G.</i>	<i>Erdogmus D.</i>
<i>Proposed</i>	1	-	-	-
<i>Polyfit I.</i>	0.815	1	-	-
<i>Haiying G.</i>	0.796	0.684	1	-
<i>Erdogmus D.</i>	0.066	0.045	0.045	1

which justifies the use of the Pearson's correlation coefficient and is a reasonable practice in biometric systems research. Table I gives such values, from where the higher similarity between the outputs given by the proposed strategy and the one of Haiying and Guoping is evident. Interestingly, Erdogmus and Dugeley showed remarkable low levels of correlation, which from our viewpoint will give the opportunity for further improvements, if both strategies are fused.

### C. Analysis of Bias

In order to analyze the errors that are predominant in the outputs given by each method, for each case we obtained a vector  $\vec{v} = (m, \theta)$ , where  $m$  is the the Euclidean distance between the estimated  $(x_e, y_e)$  and true  $(x_t, y_t)$  corner position and  $\theta$  is the arctangent of  $(x_e - x_t, y_e - y_t)$ . The relative frequency of such values is given in Figure 12, where the horizontal axes denote angle and the vertical denote

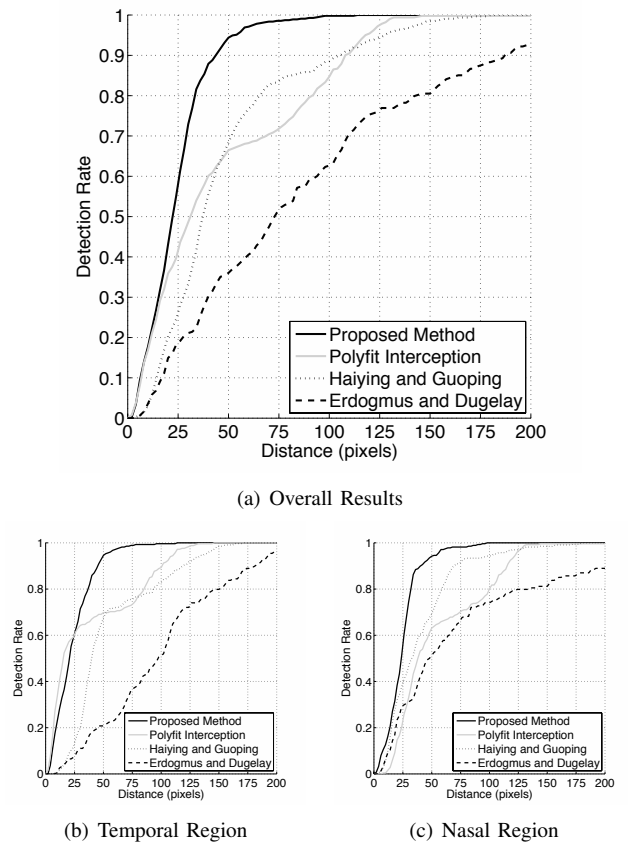


Fig. 10. Detection rate on frontal images.

magnitude. It can be observed that deviations of the proposed method and of the polynomial interpolation interceptions are homogeneously distributed in all directions, slightly deviated to the  $[0, \frac{\pi}{2}]$  interval. Considering that our datasets were composed exclusively by right eye images, this means that estimates tend to be biased NorthEast of the true eye-corners. On the nasal region, the prediction tends to be closer to the center of the eye than the true location. This fact is specially evident for the estimates of the method of Haiying and Guoping. Regarding the Erdogmus and Dugeley approach, temporal deviations were observed more sparse, with slight predominancy to the right of the true corner. For the nasal region, whereas the other methods seem to have a clear bias to the center of the face, deviations spread over all directions. This atypical behavior shown by the Erdogmus and Dugeley method on both regions is probably due to the fact that, being heavily dependent on edge detection, it is also considerably affected by data degradation. It is interesting to note that such distributions of deviations are in concordance to the observed correlation values, where a higher similarity between the proposed method, the interception of polynomials and the Haiying and Guoping methods was observed.

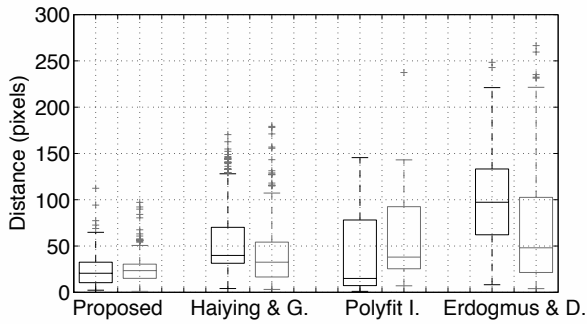


Fig. 11. Distances between the predicted corners and the true locations, on frontal images. Black and gray represent the temporal and nasal regions respectively.

#### D. Robustness to Variations in Data

Robustness is a key issue of the proposed method and we aimed to assess the decreases in performance when the quality of the data is degraded by different factors. In this analysis we decided to exclusively compare the results obtained by the proposed method to the approach of Haiying and Guoping's, as this it was the one with performance closest to ours and is considered a state-of-the-art approach. Figure 13 summarizes the obtained error values in data set, where the images were notoriously degraded by the corresponding factor. The black boxplots denote the results of our method and the gray bars those of Haiying and Guoping. From its analysis, one can conclude about the higher stability of the performance of our method across the different data sets, as average error values are steady and under 50 pixels. Oppositely, the method of Haiying and Guoping notoriously degraded its performance when handling rotated iris data, simultaneously augmenting its variance.

Figure 14 highlights such decreases in performance and gives the detection rates with respect to the error value (in pixels). Here, it is specially evident the highest slope of our method's performance plots for small errors, which may indicate that large errors in the estimates are quite unlikely, in opposition to the values observed for the other strategy.

1) *Blur*: Acquiring sharp data in less controlled acquisition environments is an issue, as slight movements of subjects often correspond to severely blurred data, in result of

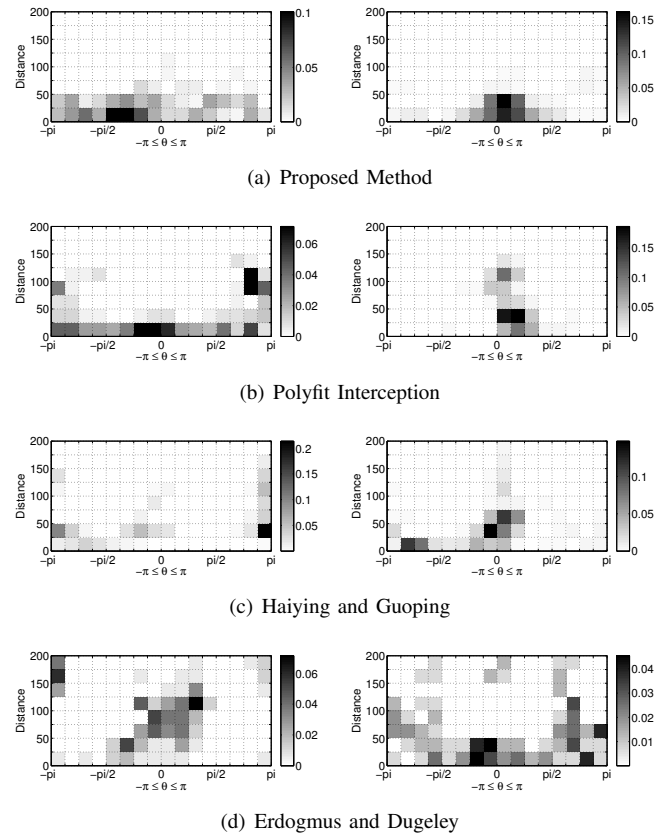


Fig. 12. Relative frequencies of the observed deviations between the predicted and true positions of eye-corners. Left and right images are for the temporal and nasal corners respectively.

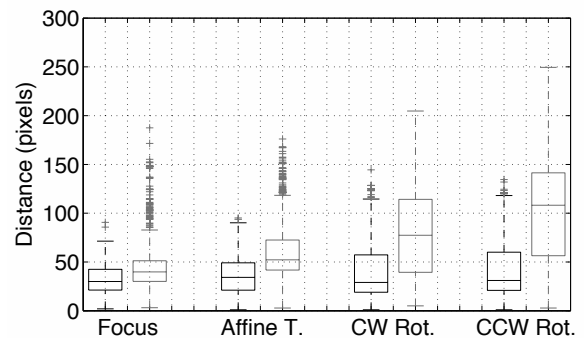
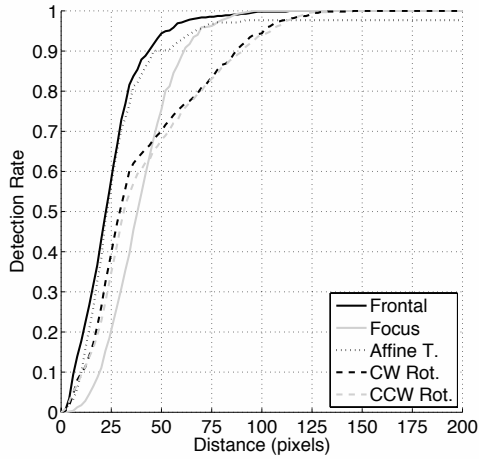
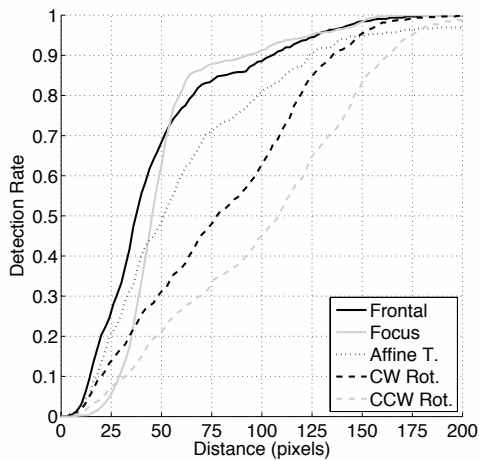


Fig. 13. Distance from the different methods outputs to the actual eye-corners on frontal images. Black and gray represent the proposed method and Haiying and Guoping's respectively.



(a) Proposed Method



(b) Haiying and Guoping

Fig. 14. Detection rate in function of the distance for all image variations.

small depth-of-focus ranges. For such, the ability of handling blurred data is a desirable property of any robust corner detection method. We observed that our method only slightly decreased its performance, whereas Haiying and Guoping's performed better in blurred data than in the focused images. The minor degradation in performance of our proposal was due to the stage that defines the ROIs, as illustrated in Figure 15: edges become less prominent in blurred data, the region growing process stops at different iterations and, consequently, the candidate search areas are also different. This, coupled with the fact that the blur also degrades the performance of the method used for the extraction of candidates, lead to a worst outcome.

2) *Deviated Gaze*: Gaze is another important factor in less controlled acquisition environments, as it is expected that most of the times, subjects head and eyes will not be aligned with the camera. In this case, we our method behave robustly, which was regarded as extremely positive and may indicate a good behavior on such type of data. Specially, there was a typical case where our method had better performance: when

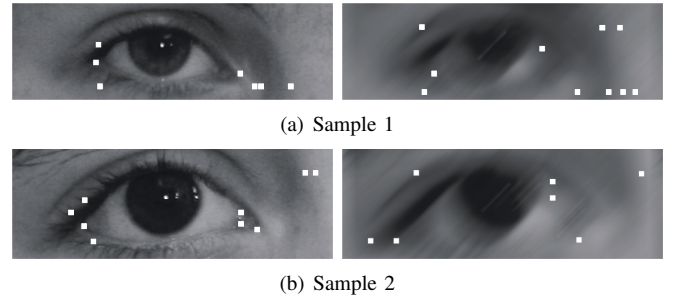


Fig. 15. Extraction of candidate points in frontal images and in the corresponding blurred versions.

images have visible background, or those with notorious facial elements (e.g., nasal bone). Figure 16 illustrates such cases and stresses the robustness of the proposed method to deviations in gaze.

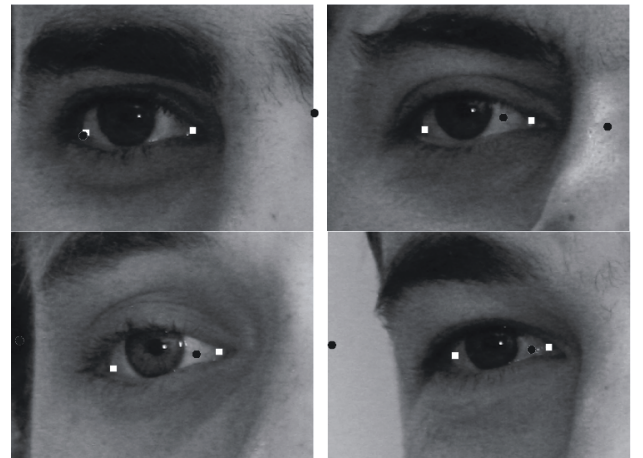


Fig. 16. illustration of the results typically obtained in gaze deviated images. White squares and black circles represent our method and Haiying and Guoping's outputs respectively.

3) *Rotation*: Rotation is another case of special interest and significant rotations in data are expected, in result of different types of movements in the uncontrolled acquisition scene. Again, our method showed a much more robust behavior than the approach of Haiying and Guoping, which significantly deteriorated its performance. We claim that this is due to the vertical and horizontal variance projection functions that produce highly different results in rotated data and, consequently, bias further processing. This is highlighted by Figure 17, where a visible predominant bias in the opposite direction of rotation can be seen. This is in opposition to our method, as illustrated in Figure 18, where a different behavior for each corner was observed: in the nasal corner, vectors counteract the direction but angles changes are minimal. Regarding the temporal corner, prediction tends to follow the rotation with a larger angle variation.

#### IV. CONCLUSIONS

Eye-corner detection concerns numerous researchers and motivated different proposals, which were observed to sig-

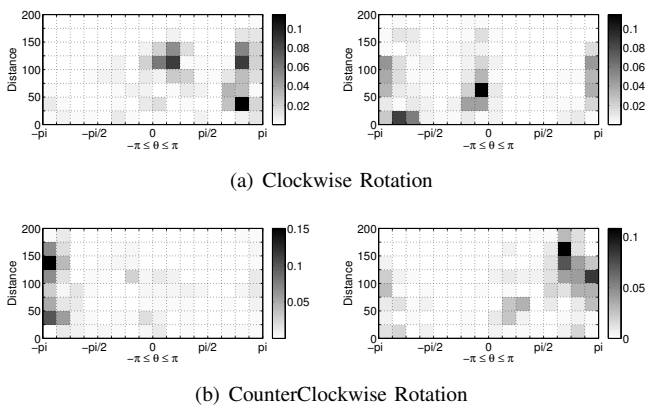


Fig. 17. Relative frequencies for the deviations of the Haiying and Guoping in rotated data. Left and right images are for the temporal and nasal regions respectively.

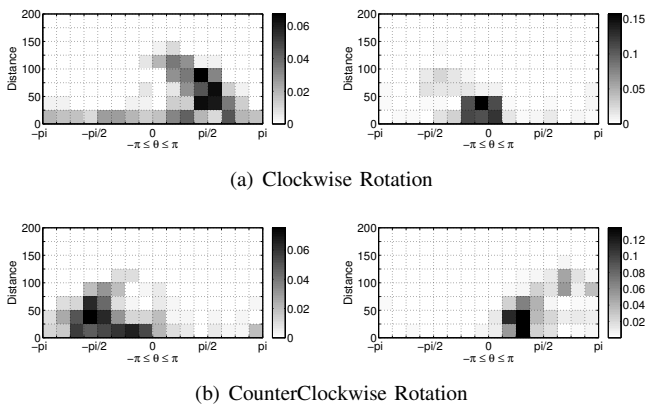


Fig. 18. Relative frequencies for the deviations of the proposed method in rotated data. Left and right images are for the temporal and nasal regions respectively.

nificantly deteriorate their performance when dealing with degraded data, acquired in less controlled setups. This gave raise to a new proposal for the detection of eye-corners in periocular images that simulate *real-world* data. We compared the results obtained by our proposal to other state-of-the-art methods and concluded that it consistently outperformed, either when operating in noise-free and degraded data (rotated, blurred, affine-transformed and with significant differences in scale). Finally, it should be stated that such improvements were obtained without significant increases in the computational demands of the task, which was also positively regarded, considering the real-time demands that usually eye-corner detection techniques have.

#### ACKNOWLEDGMENTS

We acknowledge the financial support given by “FCT-Fundação para a Ciência e Tecnologia” and “FEDER” in the scope of the PTDC/EIA-EIA/103945/2008 research project “NECOVID: Negative Covert Biometric Identification”.

#### REPRODUCIBLE RESEARCH

Here we give all the information required to reproduce the results given in this paper, either the urls from where all

the data sets can be downloaded and the MATLAB<sup>®</sup> source code developed in the scope of this research work:

- MATLAB<sup>®</sup> source code. The code implemented during the development and test of our method is available at: <http://iris.di.ubi.pt/cornerDetection/Source.zip>, pre-compiled in “.p” files, for MACOS environments.
- Data sets. A description of all the images included in any data sets used in this paper can be downloaded from <http://iris.di.ubi.pt/cornerDetection/Datasets.zip>, together with the corresponding ground-truth data.

#### REFERENCES

- [1] H. Akaike. A new look at the statistical model identification. *IEEE Transactions on Automatic Control*, 19(6):716–723, December 1974.
- [2] V. Caselles, R. Kimmel, and G. Sapiro. Geodesic active contours. *International Journal of Computer Vision*, 22(1):61–79, February 1997.
- [3] N. Erdogmus and J.-L. Dugelay. An efficient iris and eye corners extraction method. In *Proceedings of the 2010 joint IAPR international conference on Structural, syntactic, and statistical pattern recognition, SSPR/SPR’10*, pages 549–558, Berlin, Heidelberg, 2010. Springer-Verlag.
- [4] G. C. Feng and P. C. Yuen. Variance projection function and its application to eye detection for human face recognition. *Pattern Recognition Letters*, 19(9):899 – 906, 1998.
- [5] X. Haiying and Y. Guoping. A novel method for eye corner detection based on weighted variance projection function. In *CISP ’09: Proceedings of the 2nd International Congress on Image and Signal Processing*, pages 1–4, October 2009.
- [6] C. Harris and M. Stephens. A combined corner and edge detector. In *Proceedings of the Fourth Alvey Vision Conference*, pages 147–151, Manchester, 1988.
- [7] M. H. Khosravi and R. Safabakhsh. Human eye sclera detection and tracking using a modified time-adaptive self-organizing map. *Pattern Recognition*, 41:2571–2593, 2008.
- [8] J. S. Lim. *Two-Dimensional Signal and Image Processing*, pages 469–476. Prentice Hall, 1990.
- [9] P. E. Miller, A. W. Rawls, S. J. Pundlik, and D. L. Woodard. Personal identification using periocular skin texture. In *SAC ’10: Proceedings of the 2010 ACM Symposium on Applied Computing*, pages 1496–1500, New York, NY, USA, 2010. ACM.
- [10] U. Park, A. Ross, and A. Jain. Periocular biometrics in the visible spectrum: A feasibility study. In *BTAS ’09: Proceedings of the IEEE 3rd International Conference on Biometrics: Theory, Applications, and Systems*, pages 1–6, September 2009.
- [11] H. Proença, S. Filipe, R. Santos, J. Oliveira, and L. A. Alexandre. The ubiris.v2: A database of visible wavelength iris images captured on-the-move and at-a-distance. *IEEE Transactions on Pattern Analysis and Machine Intelligence*, 32:1529–1535, 2010.
- [12] M. Savvides, K. R. Jr., D. L. Woodard, and G. Dozier. Unconstrained biometric identification: Emerging technologies. *Computer*, 43:56–62, 2010.
- [13] P. Soille. *Morphological Image Analysis: Principles and Applications*, pages 173–174. Springer-Verlag, 1999.
- [14] T. Tan, Z. He, and Z. Sun. Efficient and robust segmentation of noisy iris images for non-cooperative iris recognition. *Image and Vision Computing*, 28(2):223–230, 2010.
- [15] D. Woodard, S. Pundlik, P. Miller, R. Jillela, and A. Ross. On the fusion of periocular and iris biometrics in non-ideal imagery. In *ICPR 2010: Proceedings of the 20th International Conference on Pattern Recognition*, pages 201–204, August 2010.
- [16] C. Xu, Y. Zheng, and Z. Wang. Semantic feature extraction for accurate eye corner detection. In *ICPR 2008: Proceedings of the 19th International Conference on Pattern Recognition*, pages 1–4, December 2008.
- [17] Z. Zheng, J. Yang, M. Wang, and Y. Wang. A novel method for eye features extraction. In *Proceedings of the International Conference on Computational and Information Sciences, Lecture Notes on Computer Science, vol. 3314*, pages 1002–1007, 2004.

- [18] Z. Zheng, J. Yang, and L. Yang. Semantic feature extraction for accurate eye corner detection. *Pattern Recognition Letters*, 26:2252–2261, 2005.